Materials Science & Engineering A 791 (2020) 139622

Contents lists available at ScienceDirect

Materials Science & Engineering A

journal homepage: http://www.elsevier.com/locate/msea

On the substitution of vanadium with iron in Ti–6Al–4V: Thermo-Calc simulation and processing map considerations for design of low-cost alloys

Michael O. Bodunrin [a,b,c,*], Lesley H. Chown [a,b], Josias W. van der Merwe [a,b], Kenneth K. Alaneme [b]

[a] School of Chemical and Metallurgical Engineering, DST-NRF Centre of Excellence in Strong Materials and African Materials Science and Engineering Network (AMSEN): All University of the Witwatersrand, Private Bag 3, WITS, 2050, Johannesburg, South Africa
[b] Department of Metallurgical and Materials Engineering, Federal University of Technology Akure, P.M.B. 704, Ondo State, Nigeria
[c] African Academy of Sciences, P.O. Box 24916-00502, Nairobi, Kenya

ARTICLE INFO

Keywords:
Low-cost titanium alloys
Hot working
Activation energy
Lamellar microstructure
Dynamic globularisation
Processing map

ABSTRACT

Two basic cost reducing concepts, manipulation of alloy chemistry and optimisation of the hot working process, were adopted in developing low-cost experimental titanium alloys that may be suitable for land-based applications. Iron, a low-cost beta stabilising element in titanium alloys, was used as a partial and full replacement for vanadium in ASTM grade 5 Ti–6Al–4V. Thermo-Calc simulations were first done on the Ti–6Al-*x*V-*y*Fe alloy compositions (for $y = 4 - x$ and $x = 1$–3) to predict the amounts of phases and the β-transus temperatures. Thereafter, the compacted powders of the different experimental alloys were melted and allowed to solidify in the electric arc furnace cold copper hearth. Optical and scanning electron microscopy (SEM) and X-ray diffraction (XRD) were used to characterise the alloys. Also, the hardness of the low-cost alloys was measured and compared to commercial Ti–6Al–4V. The Ti–6Al–1V–3Fe alloy was subjected to hot compression testing at various temperatures (750–950 °C) and strain rates (1-10 s^{-1}) on a Gleeble 3500 thermomechanical simulator. Processing maps and microstructural validation were used to define the most suitable processing conditions. The stress exponent and apparent activation energy were also calculated using a hyperbolic-sine equation. The results show that the low-cost alloys with partial substitution of vanadium with iron contained only α-Ti and β-Ti phases with no TiFe phase. The hardness of the alloys increased with increase in iron addition. The stress exponent "*n*" value was less than 5 indicating that flow softening was not solely driven by dynamic recovery. The optimum processing conditions for hot working were found at ~900 °C and 0.1 s^{-1} strain rate. The alloy generally had a large processing window with the softening process controlled by mechanisms such as dynamic recovery, dynamic recrystallisation of prior beta grains, and dynamic alpha lath globularisation. In the region of 750–780 °C and 1.5–10 s^{-1} an area of unstable deformation was established which should be avoided during processing. This work shows that low-cost α+β titanium alloys containing iron can be manufactured using traditional ingot metallurgy techniques and loss of material due to processing-induced defects can be minimised or avoided during primary conversion process such as forging and rolling.

1. Introduction

The production of lower-cost titanium alloys was largely driven by the need to make the alloys more competitive in many land-based applications where they were promising [1,2]. Typical land-based applications include automotive, chemical, recreational, marine, jewellery, and biomedical industries [3]. In general, good strength-to-weight ratio, excellent biocompatibility and resistance to corrosion are persuasive attributes of titanium and its alloys, making them ideal for use in such applications [3,4]. The major factor impeding the widespread use of different titanium alloys in applications other than the aerospace industry is their high cost [5,6]. Most researchers have therefore focused on finding ways to reduce the cost of titanium [7,8].

Many researchers have adopted different design concepts to achieve cost reduction during the production of titanium alloys [8–10]. They have taken into account some of the critical factors which add to the

* Corresponding author. School of Chemical and Metallurgical Engineering, DST-NRF Centre of Excellence in Strong Materials and African Materials Science and Engineering Network (AMSEN): all University of the Witwatersrand, Private Bag 3, WITS, 2050, Johannesburg, South Africa.
E-mail addresses: mic.tosin@live.com, michael.bodunrin@wits.ac.za (M.O. Bodunrin).

https://doi.org/10.1016/j.msea.2020.139622
Received 31 October 2019; Received in revised form 18 May 2020; Accepted 20 May 2020
Available online 1 June 2020

high cost of titanium alloys. To sum up, expensive alloys, difficult extraction of titanium from its mineral, high energy input for casting and heat treatment, complex and multi-staged forming techniques, difficult machining and large amounts of wasted material during manufacturing are critical factors which influence the cost of producing titanium-based products. The basic cost-reducing concepts explored by researchers include: substitution of expensive with less costly alloying elements that fulfil a similar role, optimisation of hot working and machining processes, and the adoption of powder metallurgy routes to manufacture components directly from titanium powder [11–13]. In the past few years, advances in titanium research have paved the way for the use of more robust approaches in developing low-cost titanium alloys. Notable examples of this are the FAST-*forge* process [14], Cristal Metals Armstrong process [15] and electrochemical deoxidation Metalysis Process using the Fray, Farthing and Chen process [16].

In this work, two of the aforementioned basic concepts were adopted in developing low-cost Ti–6Al-*x*V-*y*Fe. These low-cost alloys were proposed as potential alternative to Ti–6Al4V in a number of land-based applications. The concepts addressed the challenges of expensive alloying elements, as well as complex, multi-stage forming of titanium ingots. The first concept involved the replacement of vanadium, an isomorphous beta stabiliser in Ti–6Al–4V, with iron which is an inexpensive eutectoid forming beta stabiliser. The second concept was the optimisation of forming parameters using processing maps. In Ti–6Al–4V, both partial and full replacement of vanadium with iron were done to assess the effect of composition on microstructure and hardness of the alloys. Unlike in other studies [17,18] where full replacement has often been the focus, in this work more attention was paid to the alloys with partial vanadium substitution. This is because previous researchers have reported that TiFe or Ti_2Fe intermetallic compounds are readily formed in iron-containing titanium alloys if the iron content exceeds 2.5 wt% [12,19]. However, it was reported that a combination of iron and any of the isomorphous beta stabilisers e.g. V, Mo and Nb, could prevent intermetallic compounds such as TiFe or Ti_2Fe from forming in beta titanium alloys [20]. Consequently, the role of iron additions on the microstructures and hardness of the experimental Ti–6Al-*x*V-*y*Fe alloys was assessed and is presented in this work.

As part of the first phase of this work, the experimental alloys were subjected to corrosion testing in different environment. Additionally, initial compression testing was performed on the experimental alloys at a constant temperature of 900 °C and 1 s^{-1} strain rate. The results obtained from these experiments have been reported elsewhere [21,22]. Summarily, Ti–6Al–1V–3Fe offered superior corrosion resistance in 3.5 wt% NaCl and 3.5 M H_2SO_4 solutions. Also, the alloy showed lower resistance to deformation than the commercial Ti–6Al–4V due to an increase in the beta phase by Fe in Ti–6Al–1V–3Fe. The beta phase in titanium has a *bcc* structure which possesses more slip systems in comparison with the *hcp* alpha phase, hence causing lower flow stress in Ti–6Al–1V–3Fe compared to Ti–6Al–4V.

On the basis of corrosion performance and low resistance to deformation, Ti–6Al–1V–3Fe alloy was selected for further deformation studies as the second phase of this work and the results are also presented. A recent cost analysis done on the experimental alloys showed that up to 10% cost savings can be achieved from procurement of starting raw materials alone [23]. To prevent this savings from being sieved away by processing of the alloy, it became imperative to establish the most beneficial processing parameters for hot working of the alloy and the underlying mechanism. This can also save about 40% of wasted materials during forming of alloys into different profiles. The hot forming parameters of the Ti–6Al–1V–3Fe alloy have been optimised to reduce the contribution of complex and multi-stage forging processes to the high cost of titanium alloys production.

Due to their relevance to conventional ingot metallurgy which remains the oldest and one of the most prominent commercial techniques used in the production of titanium alloy components, the two cost-reducing methods adopted in this study were chosen.

2. Materials and method

2.1. Alloy design and casting

The initial prediction of phase proportions and β-transus temperatures of the targeted low-cost alloys was simulated on a Thermo-Calc software with the TTTi3 database. Based on the selected compositions, molybdenum equivalent (Mo-eq.) values of the alloys were also calculated from Equation (1) [24] since Mo-eq. of −5 to 5 wt % are by approximation classified as α+β alloys [25,26]. These values were considered in the alloy design to ensure the alloys were essentially the α+β type.

$$\begin{aligned} \mathrm{Mo}-eq.\ (wt\%) = {} & \mathrm{Mo} + 0.67\mathrm{V} + 0.44\mathrm{W} + 0.28\ \mathrm{Nb} + 0.22\mathrm{Ta} \\ & + 1.6\mathrm{Cr} + 1.25\mathrm{Ni} + 1.7\mathrm{Co} + 2.9\mathrm{Fe} - 1.0\mathrm{Al} \end{aligned} \quad (1)$$

The various compositions of the alloys were produced by mixing and compacting a predetermined mass of elemental Ti, Al V and Fe powders and then melting in a water-cooled, vacuum arc-melting furnace with a copper crucible. Prior to melting, a 5×10^{-3} bar vacuum environment was created in the melting chamber and purged with argon gas to remove oxygen. The process was repeated three times. A pure titanium sample which served as an oxygen getter was first melted to further minimise oxygen contamination before melting the alloy compacts. The as-cast samples were melted three times to homogenise the ingot compositions. The alloys were homogenised further by solution-treating at 790 °C in a muffle furnace for 4 h followed by air-cooling.

2.2. Hot compression testing

The axisymmetric compression samples were machined from the experimental Ti–6Al–1V–3Fe alloy casting with rectangular axial dimensions of 8 × 8 × 12 mm. Using a Gleeble 3500® thermomechanical simulator, single-hit axisymmetric hot compression tests were conducted on the experimental alloy up to a strain of 0.6. The compression tests were done at the deformation temperatures of 750 – 950 °C in steps of 50 °C and strain rates of 0.001, 0.01, 0.1, 1 and 10 s^{-1}. Before testing, a spot welder was used to solder a chromel-alumel thermocouple to the midspan of the samples. During compression testing the thermocouple measures the temperature of the samples. At a heating rate of 5 °C.s^{-1} the samples were heated directly to the targeted temperature of deformation. The samples were then kept for 180 s at this temperature to achieve uniform sample temperature. Thereafter, the samples were force cooled in compressed air. Only samples with the barrelling coefficient that was <1.1 [27] after compression were considered valid.

The flow stress data obtained from the experiments were used to determine the constitutive constants at the peak stress. Also, the data was used to construct processing map at the total strain of 0.6. An Arrhenius equation with a hyperbolic-sine function and a temperature-compensated strain rate parameter (Zener-Hollomon parameter) [28] was used to calculate the apparent activation energy and stress exponent [29,30]. In Equations (2)–(4), the constitutive relations are expressed, and the constitutive constants were used to indicate the mechanisms governing the process of deformation.

$$\dot{\varepsilon} = f(\sigma)\exp\left(\frac{-Q}{RT}\right) \quad (2)$$

$$Z = \dot{\varepsilon}\exp\left(\frac{Q}{RT}\right) \quad (3)$$

and:

$$f(\sigma) = \begin{cases} A_1\sigma^n, & for: \ \alpha\sigma < 0.8 \\ A_2\exp(\beta\sigma_p), & \alpha\sigma > 1.2 \\ A_3\left[\sinh(\alpha\sigma_p)\right]^n & for\ all\ \sigma \end{cases}$$

$$\dot{\varepsilon} = A_3\left[\sinh(\alpha\sigma_p)\right]^n \exp\left(\frac{-Q}{RT}\right) \quad (4)$$

where $\sigma_p$is the peak stress, $\dot{\varepsilon}$ is strain rate, Q is the activation energy, n is the stress exponent, T is temperature (in °C) R is the universal gas constant (8.314 kJ/mol), Z is the Zener-Hollomon parameter, and α, β, A_1, A_2 and A_3 are material constants.

Processing map was developed in accordance with the procedures described by Prasad et al. [31]. This involves the overlaying of instability map on the power dissipation map. The power dissipation efficiency (η) was derived exclusively from the strain rate sensitivity parameter following equations (5) and (6) [32]. The strain rate sensitivity parameter (m) is the slope of $\ln\sigma$ *vs.* $\ln\dot{\varepsilon}$.

$$m = \frac{\partial \ln \sigma}{\partial \ln \dot{\varepsilon}} \quad (5)$$

$$\eta = \frac{2m}{m+1} \quad (6)$$

The data for constructing the instability map was obtained using Equation (7) that was proposed by Murty et al. [33,34]. This equation is one of the mostly utilised instability criteria used in predicting region of unstable deformation on the processing map of most metallic alloys.

$$\xi(\dot{\varepsilon}) = \frac{2m}{\eta} - 1 < 0 \quad (7)$$

Based on its reliability, this criterion was chosen to predict unstable regions for a wide range of metallic alloys [35].

The optical and SEM images obtained from selected deformed samples were analysed to confirm the patterns observed on the flow curves and the processing map predictions. The procedure for obtaining the micrographs is presented in Section 2.3.

2.3. Microstructural examination, X-ray diffraction and hardness testing

A Zeiss Sigma field emission gun-scanning electron microscope (FEG-SEM) and a Leica DM 6000 optical microscope were used to analyse as-cast, homogenised and compression tested samples. Prior to microstructural examination, silicon carbide abrasive paper of different grit sizes (600–4000 grit) were used in grinding the surface of the samples. Thereafter, the samples were chemo-mechanically polished using a 0.050 μm colloidal silica suspension containing 20% hydrogen peroxide. The polished samples were then etched using standard Kroll's reagent and were cleaned with ethanol in an ultrasonic bath before drying with compressed air. The FEG-SEM was equipped with an Oxford energy dispersive X-ray (EDX) detector which was used to verify the compositions of the alloys. The samples selected for EDX analyses were not etched to ensure the elemental composition was accurately measured. Back-scattered electron (BSE) imaging at 15 kV and Secondary electron (SE) imaging was also performed on the FEG-SEM to distinguish the phases present in the alloys.

Using a Bruker D2 Phaser® diffraction machine fitted with a cobalt Kα radiation source, XRD measurements were taken at 2Θ angles of 10–110°. The machine was operated at generator settings of 30 kV and 20 mA at a temperature of 25 °C. The patterns obtained were analysed using PANalytical (v3.0e) X'pert Highscore software.

A Future-Tech FM 700 microhardness testing machine was used to perform Vickers microhardness tests (HV0.3) on the homogenised samples. Measurements of hardness were repeated five times and the mean values, and the corresponding standard deviations were determined.

3. Results

3.1. Effects of iron addition

3.1.1. Phase predictions from Thermo-Calc simulation

Table 1 presents the phase proportions and beta transus temperatures obtained from Thermo-Calc simulations. The raw Thermo-Calc curves are presented in the supplementary data. The molybdenum equivalent values of the alloys obtained using Equation (1) are also listed in Table 1. The trend to note in Table 1 is that β-transus decreased as the iron content increased, while the beta-phase and molybdenum equivalent values increased. This trend concurs with established knowledge on the role that iron plays in titanium alloys. Iron being a strong beta stabilising element in titanium, a decrease in the β-transus temperature would expectedly increase the molybdenum equivalent with increasing iron addition [36]. The beta stabilising factor of iron is twice as strong as molybdenum and four times stronger than vanadium [36]. It is however established that the formation of intermetallic compounds such as Ti_2Fe and TiFe is possible depending on the iron content of titanium alloys [17,37]. These intermetallic compounds are the equilibrium phases that are formed when iron is added to titanium in considerable amounts, and they often have deleterious effects on the mechanical properties, mainly ductility and toughness [8,11,17,18,37].

The results obtained from the Thermo-Calc simulations did not show the formation of any intermetallic compounds for the selected compositions, which agrees with earlier work [20] that the use of isomophous and eutectoid beta stabilising elements together could help prevent the evolution of intermetallic compounds in iron-containing titanium alloys. However, it is still possible that segregation of iron during melting and casting of the alloys could lead to the formation of TiFe and Ti_2Fe. Consequently, the alloys were characterised to identify the phases present in the alloys. The results obtained are presented in the subsequent sections.

3.1.2. Microstructure and XRD patterns of the cast annealed alloys

Table 2 shows the average compositions of the Ti–6Al-*x*V-*y*Fe alloys subjected to EDX analyses. The composition of the alloys was close to the targeted nominal compositions. EDX was also used to identify the individual phases in the alloys. Representative EDX point analyses of the dark and light phases are presented in Fig. 1 and Table 3. The dark phase contains Ti, Al and V, but no Fe, while the light phase has Ti, Al, V and Fe. The presence of Fe in the elemental composition of the light phase established that the light phase is the beta phase. The same approach was adopted by Safdar et al. [38] when identifying the phases in selective laser melted titanium alloys. They reported that Fe was absent in the alpha phase due to its low solubility, and Fe preferentially stabilises the beta phase where it has higher solubility. The maximum solubility of Fe in β-Ti is approximately 22 wt% [39,40].

Fig. 2a shows the selected optical micrograph of the low-cost alloy, the remaining micrographs of the alloy in the as-cast and homogenised condition are available in the supplementary material. All the alloys have Widmanstätten α-laths embedded in the large beta grains. The average size of the large prior beta grains was less than 600 μm, which is consistent with the size of the α+β titanium alloys previously reported by Lütjering and Williams [20]. In Fig. 2b which show the SEM-BSE image of the experimental alloy, it is seen that the alpha laths (dark) are separated by interplatelet beta (light).

From the XRD pattern (Fig. 3), the dominant phases in all the alloys were α-Ti (hcp), β-Ti (bcc) and TiO_2. Other minor phases that were detected in the experimental Ti–6Al–4Fe and commercial Ti–6Al–4V were $FeTiO_3$ and V_2O_5 respectively. The presence of FeTiO3 suggests that intermetallic TiFe may have formed and oxidised in the alloy Ti–6Al–4Fe, where the content of vanadium was completely replaced by iron. The crystallographic data of the phases detected are given in Table 4.

Table 1
Thermo-Calc results for the Ti–Al–V–Fe alloys using the TTTi3 titanium database.

Samples	Targeted composition (wt %)				β-transus temp (°C)	Phases present at 800 °C (mol %)		Molybdenum Equivalent (wt %)
	Ti	Al	V	Fe		α-Ti (hcp)	β-Ti (bcc)	
Ti–6Al–4V	90	6.0	4	0	944	86	14	−3.32
Ti–6Al–3V–1Fe	90	6.0	3	1	937	75	25	−1.09
Ti–6Al–2V–2Fe	90	6.0	2	2	932	68	32	1.14
Ti–6Al–1V–3Fe	90	6.0	1	3	925	61	39	3.37
Ti–6Al–4Fe	90	6.0	–	4	921	55	45	5.60

Table 2
Average compositions of Ti–6Al-*x*V-*y*Fe alloys determined by EDX.

Sample	Nominal (wt %)				Actual (wt %)			
	Ti	Al	V	Fe	Ti	Al	V	Fe
Ti6Al4V w	90	6	4	–	89.9	6.0	4.1	–
1	90	6	3	1	89.8 ± 0.1	5.7 ± 0.1	3.7 ± 0.1	0.8 ± 0.1
2	90	6	2	2	89.4 ± 0.3	5.6 ± 0.1	2.7 ± 0.1	2.3 ± 0.3
3	90	6	1	3	89.1 ± 0.2	5.7 ± 0.2	1.9 ± 0.1	3.3 ± 0.1
4	90	6	–	4	89.4 ± 0.3	5.9 ± 0.1	–	4.7 ± 0.2

3.1.3. Hardness

Fig. 4 shows the increased hardness of the Ti–6Al-*x*V-*y*Fe alloys with an increase in Fe content except in Ti–6Al–2Fe and Ti–6Al–1V–3Fe where similar hardness values have been achieved. The increased hardness with Fe content can be ascribed to the solid solution strengthening effect of iron caused by the difference in the atomic radii of iron and titanium [40]. Another factor which may have contributed to the hardness of the alloys is the level of dissolved interstitials such as oxygen, nitrogen and carbon [41,42], which was not measured. As shown from the XRD results (Fig. 5), TiO_2 and iron-titanium-oxide peaks indicated the presence of oxygen in the alloy. While there is expected to be oxygen in titanium alloys, further contamination could have occurred during melting, casting and annealing of the alloys despite the precautions taken.

Table 3
Composition of α and β phases by EDX, in wt%.

Elements	α-Ti	β-Ti
Al	6.0 ± 0.1	4.0 ± 0.4
Ti	91.6 ± 0.1	81.4 ± 0.8
V	2.4 ± 0.2	8.9 ± 0.5
Fe	–	5.7 ± 0.5

3.2. Hot working behaviour of Ti–6Al–1V–3Fe

The flow behaviour, constitutive parameters, processing maps and

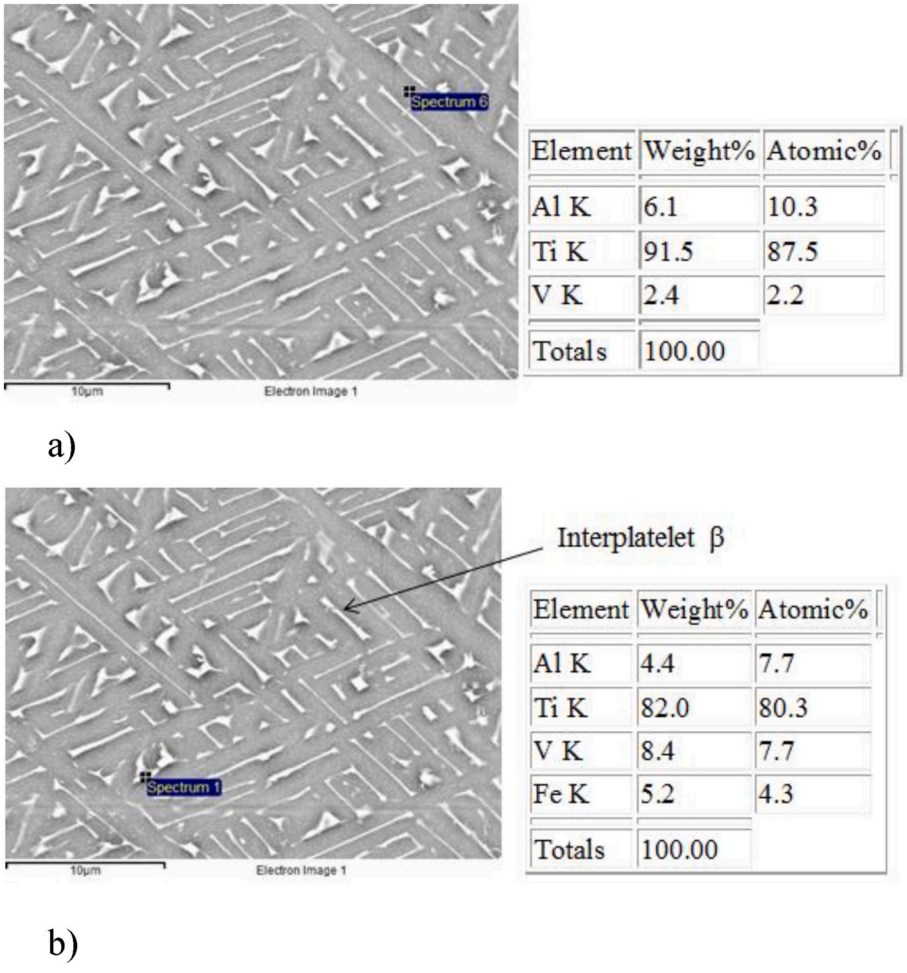

Fig. 1. EDX spot analysis of a) α phase and b) β phase in Ti–6Al–3V–1Fe.

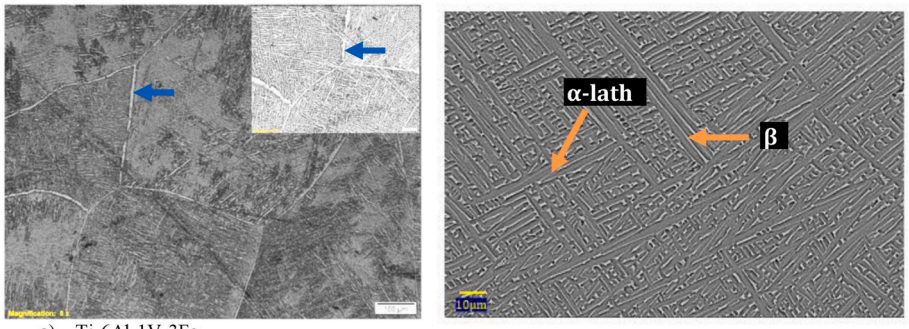

a) Ti-6Al-1V-3Fe b) Ti-6Al-1V-3Fe

Fig. 2. Microstructural features of low-cost alloy (a) optical image showing prior beta grains (blue arrow) and (b)SEM-BSE image showing α laths (dark) and retained interplatelet β (light). (For interpretation of the references to colour in this figure legend, the reader is referred to the Web version of this article.)

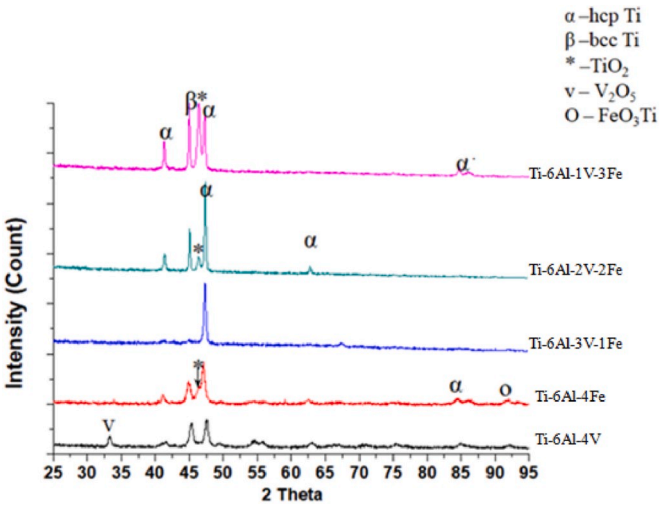

Fig. 3. XRD patterns of Ti–6Al-*x*V-*y*Fe and wrought Ti–6Al–4V alloys.

microstructural evolution of Ti–6Al–1V–3Fe are presented in this section.

3.2.1. Flow behaviour

Selected flow curves obtained from the axisymmetric compression testing of Ti–6Al–1V–3Fe alloy at the applied deformation temperatures and strain rates are presented in Fig. 5, the entire flow curves are made available in the supplementary data. The general trend that can be observed is that the flow stress has a direct relationship with strain rate since the stress increased with increasing strain rate. However, inverse relationship exists between flow stress and deformation temperature as flow stress decreased as deformation temperature rose. An increase in strain rate will cause an increase in the speed of mobile dislocations, as well as an increase in flow stress. These relationships have been explained [43] in Equations (8) and (9):

$$\dot{\varepsilon} = \rho b A \sigma^m \tag{8}$$

$$v = A\sigma^m \tag{9}$$

where $\dot{\varepsilon}$ is strain rate, v is average dislocation velocity, b is Burgers vector, ρ is dislocation density, A is a constant, σ is flow stress and m is strain rate sensitivity parameter [44].

At low strains <0.05 there was a rapid increase in flow stress (Fig. 5). This was due to generation and multiplication of dislocations which work hardened the material [45]. As the strain increase beyond 0.05, the flow stress dropped continuously or assumed a near steady-state due to flow softening. Balasubrahmanyam and Prasad [46] and Zhang et al. [47] reported similar trends in hot worked titanium alloys. Continuous flow softening occurs when the work hardening rate is exceeded by rate of softening, while steady-state flow stress is observed when the rate of work hardening is at equilibrium with flow softening rate [48].

The distinct trends observed on the flow curves in Fig. 5 include continuous flow softening at temperatures below 950 °C for all strain rates. However, at 950 °C and all strain rates, the flow stress attained a near steady-state after the peak stress was reached. Broad peaks were observed for all temperatures at a strain rate of 10 s^{-1} which became narrower at lower strain rates.

At all deformation temperatures, the flow curves of samples deformed at 1 s^{-1} showed slight oscillations, while the samples deformed at 0.01 and 0.001s^{-1} showed discontinuous yielding. This behaviour was quite apparent at 0.01 s^{-1} strain rate, with a rapid increase in flow stress until a sharp distinct peak at a very low strain, followed by a second peak prior to flow softening. Discontinuous yielding has not been reported in pure titanium or commercial Ti–6Al–4V hot-worked in the beta phase region, but has been found in beta titanium alloys [46,49]. The magnitude of discontinuous yielding has been attributed to the concentration and type of the beta stabilising elements [24,50].

However, in this work, the discontinuous yielding was not caused by microstructural phenomena, but was due to a change in strain rate at a low strain of ~0.02 as presented in Fig. 6. The high strain rates at the start of deformation, 0.06 s^{-1} as compared to 0.01 s^{-1}, led to the sharp initial peaks observed on the flow curves. This change in strain rate was noticeable when all the alloys were compression tested at ≤ 0.01 s^{-1}. Although the overall strain rate was not affected, the misleading initial peaks were not a consequence of microstructural responses to the imposed parameters but were likely due to variations in the hydraulic motion regulating the compression jaws.

The shape of the flow curves was used to suggest the different

Table 4
Crystallographic data of phases present in the as-cast and annealed alloys.

Phase	Space group no.	*a* (Å)	*b* (Å)	*c* (Å)	Cell vol. (10^6 p.m.^{3})	Reference No.
α-Ti (hcp)	*P63/mmc* (194)	2.9505	2.9505	4.6826	35.30	044–1294
β-Ti (bcc)	*Im-3m* (229)	3.3065	3.3065	3.3065	36.15	044–1288
TiO_2 (orthorhombic)	*Pbnm* (62)	4.9010	9.4530	2.9580	137.04	049–1433
FeO_3Ti (Rhombohedral)	*R-3* (148)	5.0884	5.0884	14.093	316.01	029–0733
V_2O_5 (Tetragonal)	*P E*	14.2590	14.2590	12.576	2556.94	045–1074

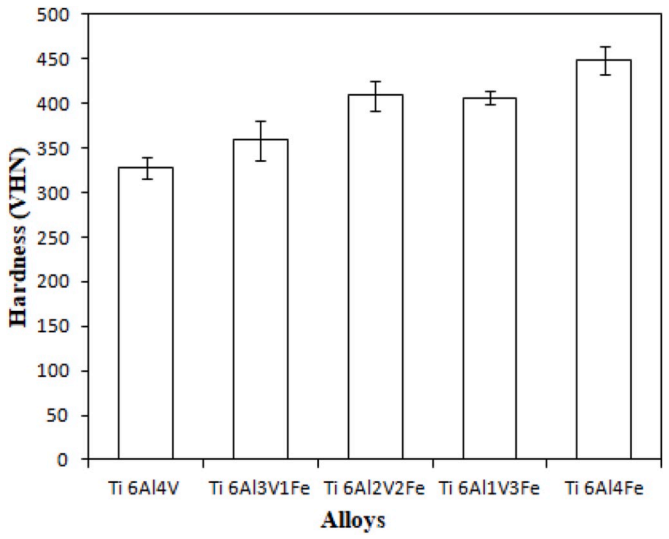

Fig. 4. Vickers microhardness of Ti–6Al–4V and Ti–6Al-*x*V-*y*Fe alloys.

softening mechanisms that dominate the deformation of metals and alloys [51,52]. The flow curves in Fig. 5 show strain hardening by increasing stress at low strains. Broad peaks were also observed at a high strain rate of 10 s^{-1}, attributable to dynamic recrystallisation or globularisation of either one or both constituent phases. The steady-state stress at the highest temperature of deformation could be due to dynamic recovery or superplasticity, while continuous flow softening at lower temperatures could be due to dynamic globularisation. or manifestation of flow instabilities, such as cracking, void formation or adiabatic shear bands. Continuous softening indicates dynamic globularisation of titanium alloys with either a fully lamellar or an acicular pre-form microstructure [53,54]. The oscillations at 1 s^{-1} could be due to dynamic recrystallisation or cracking in the material [55]. Since the flow curve is not able to provide a more definite mechanism controlling the softening during the entire deformation process, further analyses would be needed to substantiate the dominant softening mechanism(s) of the alloys during hot working.

3.2.2. *Constitutive constants and processing map*

Constitutive constants and processing maps can provide further insights into the mechanisms controlling the deformation process. The processing map can help to predict the region of stable and unstable deformation. However, to obtain a more accurate prediction from this map, the flow stress obtained from the experiments has to be corrected for adiabatic heating and frictional effects. The barrelling coefficients of the deformed samples were calculated and were used as an acceptance criterion to validate the experiment. All accepted compression tests had barrelling coefficients that were less than the maximum permissible limit of 1.1 [27]. Friction correction was therefore not performed, as the nickel paste and graphite foil applied between the samples and the ISO-T tungsten carbide anvils offered adequate lubrication to reduce friction during deformation. Adiabatic heating occurred at strain rates 1 and 10 s^{-1} and at test temperatures below 900 °C. The correction of flow stress was done in accordance with previous work [56,57] and the corrected stresses were used for the constitutive constants and processing map.

The constitutive constants derived at the peak stress values only are listed in Table 5. The plots showing how the different constitutive values were obtained are presented in the supplementary material. The activation energy and the stress exponent values have been used to suggest flow softening mechanisms during deformation. The activation energy obtained in this study is within the typical range for hot working of α+β titanium [58,59]. However, since it is an apparent value, it is impossible to ascribe any physical meaning to the activation energy [60,61]. The stress exponent is usually taken to be 5, should the deformation process be controlled by dislocation climb and glide i.e. dynamic recovery [62,63]. From Table 5, the stress exponent value was less than 5, implying that mechanisms other than dynamic recovery contributed to flow softening during hot working of the Ti–6Al–1V–3Fe [63]. This supports the trends observed on the flow curves where dynamic recrystallisation was identified as a probable softening mechanism.

Fig. 7 shows the processing map for Ti–6Al–1V–3Fe constructed at a strain of 0.6. The map shows a large processing window within the tested strain rate and deformation temperature conditions. However, a small region of instability was found at 770–780 °C/1.5–10 s^{-1} on the map. This region should be avoided while the alloy is being worked. The power dissipation values on the processing map range from 10 to 50% with the largest region of the map having a dissipation efficiency of at least 30%. This means that the primary mechanism governing the deformation process is dynamic recrystallisation. The optimum set of conditions for hot working as predicted by the processing map was found at approximately 900 °C and 0.1 s^{-1} where the highest dissipation efficiency of 50% was found. This region is marked “A” on the map.

The microstructures of samples deformed under conditions creating unstable and stable regions were analysed for validating the prediction of the processing map. Fig. 8 displays the optical and SEM image representations of the samples. The yellow dotted lines in Fig. 8a indicate equiaxed prior beta grains while the red solid rings in Fig. 8b and d indicate voids and cracks. Equiaxed prior beta grains is seen in Fig. 8a while crack is seen in the vicinity of deformation bands in Fig. 8b. The equiaxed prior beta grains are signs of dynamic recrystallisation while the cracks confirmed unstable deformation as predicted by the processing map. The SEM image taken at a higher magnification than the optical micrographs did not capture the equiaxed prior beta grains (Fig. 8c) but did clearly show defects -voids and cracks (Fig. 8d).

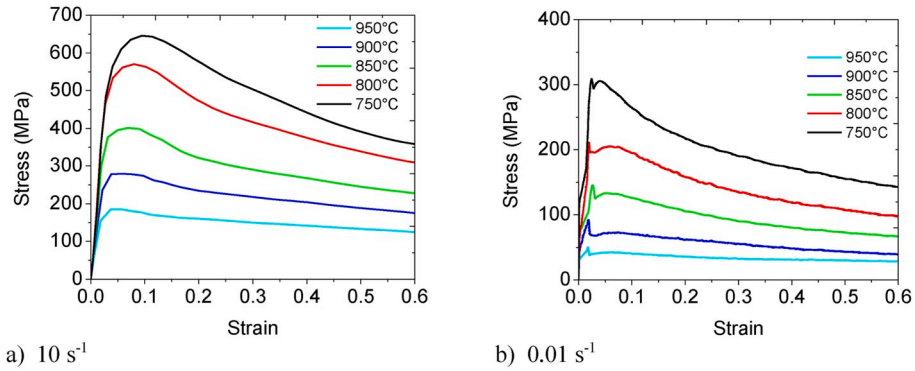

Fig. 5. Flow stress curves obtained by rectangular axial compression testing of Ti–6Al–1V–3Fe in the temperature range of 750–950 °C and at strain rates of (a) 10 s^{-1} and (b) 0.01 s^{-1}.

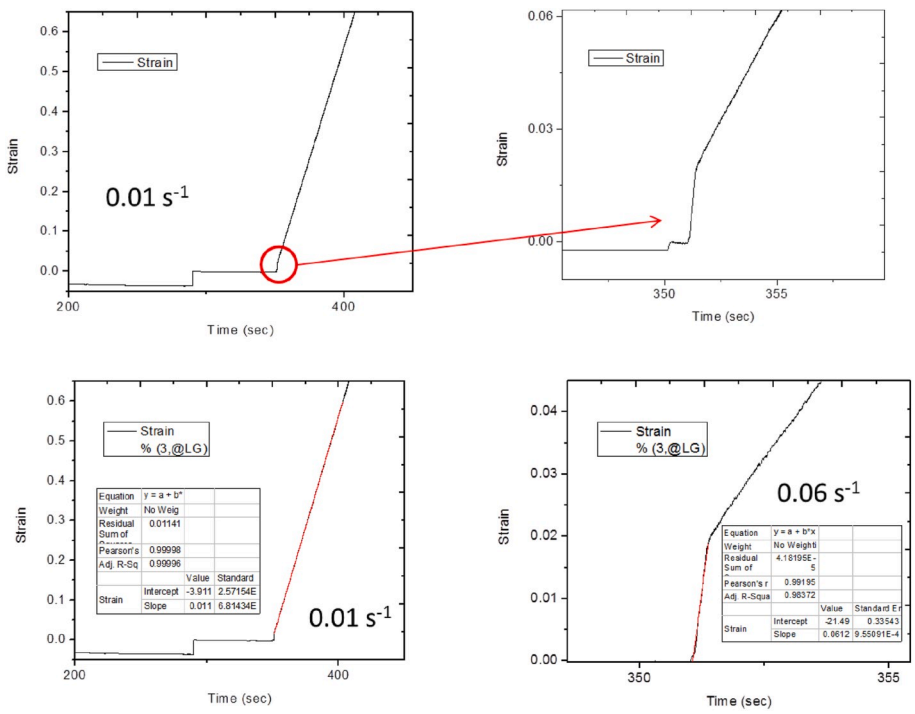

Fig. 6. Strain versus time profile for Ti–6Al–1V–3Fe deformed at 850 °C and 0.01 s^{-1} showing the increase in strain rates at low strain (~0.02).

Table 5
Constitutive constants for hot working of Ti–6Al–1V–3Fe.

B	ń	α (MPa^{-1})	n	S	Q ($kJmol^{-1}$)	A (s^{-1})
0.03	5.595	0.006	3.808	15.389	487	1.50×10^{21}

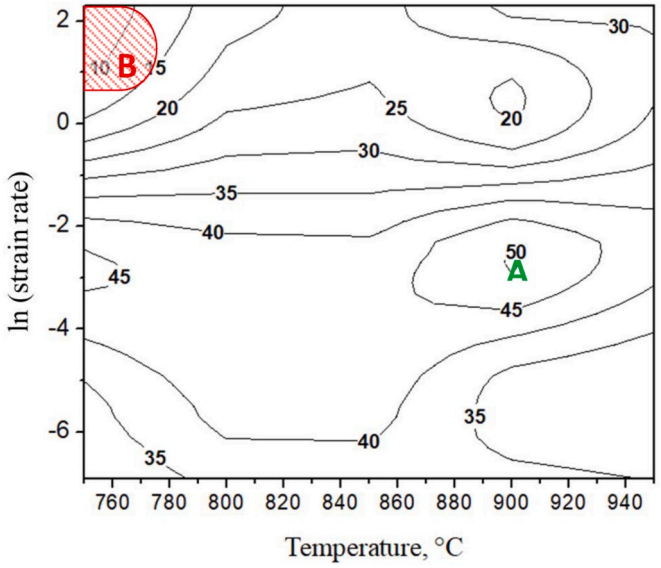

Fig. 7. Processing map for Ti–6Al–1V–3Fe at a total strain of 0.6. The red region is region of unsafe deformation; A is the safe region with the highest dissipation efficiency. (For interpretation of the references to colour in this figure legend, the reader is referred to the Web version of this article.)

3.3. Evolution of microstructures in hot-worked Ti–6Al–1V–3Fe

The microstructures of selected deformed samples tested at different strain rates and deformation temperatures were examined to understand their effects on the evolved microstructures.

Fig. 9 shows the selected SEM-BSE images of Ti–6Al–1V–3Fe alloy deformed at different strain rates and deformation temperatures. The microstructures of samples deformed at 750 °C/10 and 1 s^{-1} (Fig. 9a and c) exhibited severe bending and rotation of α laths (black arrow), with defects such as voids and cracks very conspicuous at 10 s^{-1}. These microstructural features are diagnostic of poor workability under warm working (700°□) and high strain rates. Secharchayulu et al. [64] made similar observation during hot working of Ti–6Al–4V with an initial lamellar microstructure. Prominent cracks were found at the prior beta grain boundaries and they explained that the localised cracking was promoted by stress concentration at the prior beta grain boundaries due to sliding of the soft beta phase.

As the deformation temperature increased above 800 °C (Fig. 9b and c), the bending and rotation of the lamellar structures decreased, and defects were not detected at these temperatures. The reduction in the degree of lath rotation and bending with increasing temperature was attributed to the increased mobility of dislocations with increasing temperature [65].

The power dissipation efficiency values obtained from the processing map (Fig. 7) at temperatures between 800 °C and 950 °C corresponded with dynamic recovery. At temperatures below 800 °C, the movement of dislocations generated at high strain rates was restricted, as found by Fan et al. [65]. This may have caused shearing which bent and rotated the laths. At the highest deformation temperature of 950 °C (Fig. 9c), traces of fractured lamellae were seen which indicated that dynamic globularisation could have started. However, dynamic globularisation was limited by the high strain rate of 10 s^{-1}. Therefore, the dominant softening process in this region would be dynamic recovery, which was seen at 950 °C/10 s^{-1} (Fig. 9c). The microstructural features concur with the prediction of the processing map, which showed a power dissipation efficiency of ~30% and also with the near steady-state flow stress shown in Fig. 5a.

According to the processing map, the optimum processing condition for deforming Ti–6Al–1V–3Fe to a total strain of 0.6 was at 0.1 s^{-1} and 900 °C. Therefore, it became imperative to assess the microstructural evolution at this strain rate. Bending and rotation of laths was evident at

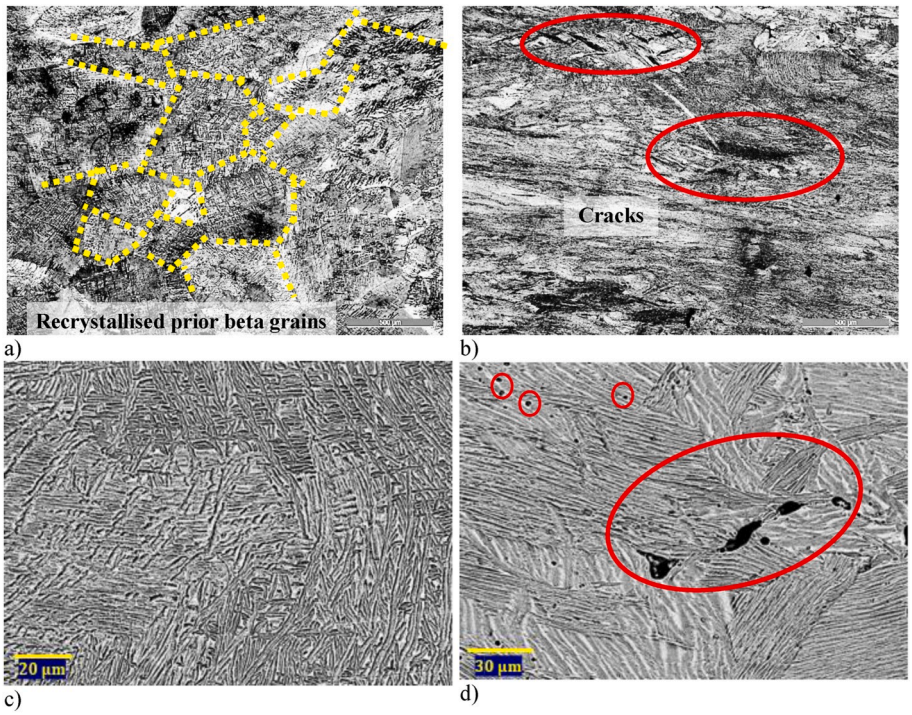

Fig. 8. Final microstructure of Ti–6Al–1V–3Fe deformed samples. Stable deformation: 900 °C and 0.1 s^{-1}: a) optical c) SEM-BSE, Unstable deformation: 750 °C and10 s^{-1}: b) optical and d) SEM-BSE.

750 °C, but this decreased as the deformation temperature increased. This was due to increased mobility of dislocations at higher deformation temperatures [65]. As shown in Fig. 8a, dynamic recrystallisation of the prior beta grains was found as the softening mechanism at the optimum processing condition. This explains why dynamic globularisation of α lamellae was hardly observed when there was a decrease in strain rate from 10 to 0.1s^{-1}. The reduction in both defects and the severity of lath rotation with decreasing strain rate indicated that workability of the alloy was improved at low strain rates. Prasad and Seshacharyulu [66], Polleti et al. [67] and Balasundar et al. [68] reported that hot working of titanium at lower strain rates and higher deformation temperatures improved the intrinsic workability of titanium alloys. This is confirmed in Fig. 9e for Ti–6Al–1V–3Fe deformed at 950 °C and 0.1s^{-1} where the alpha globules are signs of dynamic globularisation. The degree of dynamic globularisation was higher at 0.1 s^{-1} strain rate in comparison with 10 s^{-1} strain rate.

Using the additional SEM-BSE images of deformed Ti–6Al–1V–3Fe samples provided in the supplementary data, the influence of changing strain rate and constant temperature of 900°□ on the microstructural evolution of deformed Ti–6Al–1V–3Fe was assessed. It was observed that the lamellae were serrated at a strain rate of 10 s^{-1}, while bending and rotation of laths were evident at 1 s^{-1}. Serrated, bent and kinked laths are all precursors to dynamic globularisation [69,70]. Perumal et al. [71] reported that lath rotation and bending in Ti–6Al–4V with an acicular initial microstructure was largely influenced by strain, and was independent of the initial lath thickness. In this work, the total strain was kept constant for all the deformed samples, but the strain rate effect on lath rotation and bending was visible. At the strain rate of 0.1 s^{-1}, a minute amount of lath bending was seen in Ti–6Al–1V–3Fe and there were no signs of dynamic globularisation. However, there was significant dynamic globularisation at lower strain rates typically 0.01 s^{-1} and 0.001 s^{-1}. This was confirmed by the fragmentation of α lamellae into globules as shown in Fig. 9e.

4. Discussion

The efforts of researchers to reduce the cost of producing titanium alloys have evolved from the basic considerations of manipulating alloy chemistry and optimising hot working and machining to robust process modification as evident in the FAST *forge* process [14] and Fray, Farthing and Chen process [16] where final components are produced directly from titanium powder in very few steps. While these processes are very promising, their full commercialised production may take some time. Additionally, there may be limitations on the size and geometry of profiles that can be produced through these processes.

Consequently, this work has adopted two basic concepts in answering two important questions:

- How does the partially substituted vanadium with iron affect microstructure and hardness of the low-cost alloys?
- What are the optimum processing conditions and how do they differ from established conditions for commercial Ti–6Al–4V and other α+β titanium alloys?

The presented results show that partial replacement of V with Fe did not cause TiFe formation in the 1 wt% V - 3 wt% Fe alloy. This intermetallic is a major concern when Fe is added to Ti. Rather, only alpha and beta phases were detected in the alloy, with minor amounts of oxides. Thermo-Calc simulations predicted that the formation of TiFe is unlikely in the Ti–6Al-*x*V-*y*Fe alloys. Instead, the beta phase proportion would increase since iron is notably a strong beta stabiliser. The microstructures and XRD results show that there was no TiFe phase in the alloys. Although the phase proportions in the alloys were not quantified, the relative height of the main beta peak increased with increasing Fe addition. This suggests that the amount of beta phase increased with Fe addition, as predicted by the Thermo-Calc simulation. Nochovnaya et al. [19] reported that to produce iron-containing titanium alloys that are free of TiFe or Ti_2Fe, the Fe content must not exceed 2 wt%. Conversely, Ebestan et al. [17] showed that it was possible to produce TiFe or Ti_2Fe free titanium alloys via powder metallurgy. The results obtained in this

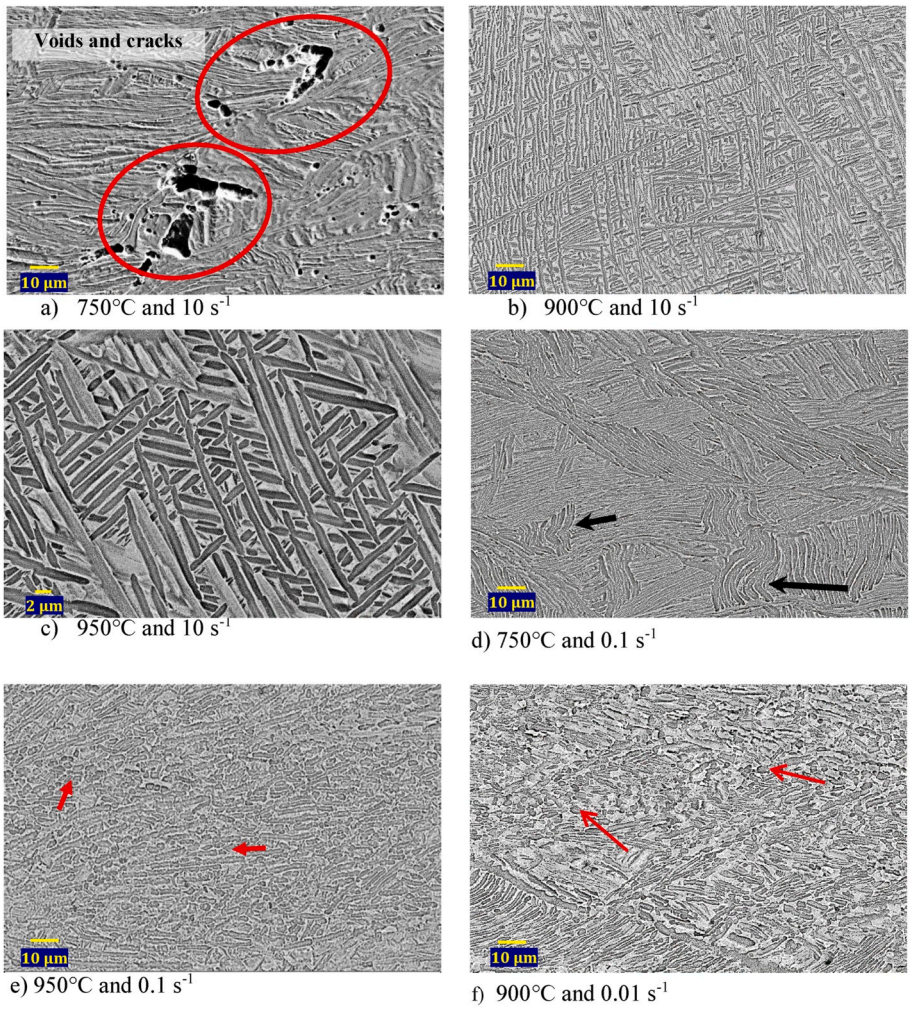

Fig. 9. Selected SEM images at different strain rates and deformation temperatures (a) 750°C and 10 s^{-1} (b) 900°C and 10 s^{-1} (c) 950°C and 10 s^{-1} (d) 750°C and 0.1 s^{-1} (e) 950°C and 0.1 s^{-1} and (f) 900°C and 0.01 s^{-1}. Black arrows show lath bending and red arrows show globular α; (a) analysed in SE mode while (b–e) were analysed in BSE mode. (For interpretation of the references to colour in this figure legend, the reader is referred to the Web version of this article.)

study have shown that use of the combination of V and Fe may prevent the formation of intermetallics even with conventional casting methods.

The higher hardness of the experimental alloys over wrought Ti–6Al–4V could be explained in terms of microstructure and iron content. The experimental alloys have a Widmanstätten structure, but the wrought Ti–6Al–4V, shown elsewhere [64], had near-equiaxed alpha and elongated alpha grains, with intergranular beta. The basket-weave microstructure of the experimental alloys would pose more resistance to dislocation movement, resulting in the higher hardness [42]. Additionally, Fe offers a higher solid solution strengthening effect than V since there is larger difference in the atomic radii of Fe and Ti compared to V and Ti [22]. In this work interstitial contents were not analysed, so it is insufficient to conclude that iron alone was responsible for the higher hardness observed in the experimental alloys. It is well-documented that oxygen, nitrogen and carbon raise the working temperatures and the hardness of both alpha and beta titanium alloys [72,73].

The results obtained from the hot working studies showed that the most advantageous parameters for working the alloy were ~900 °C working temperature and 0.1 s^{-1} strain rate. The large processing window seen on the processing map indicated the easy working of the Ti–6Al–1V–3Fe alloy. The agreement between flow curves analysis, stress exponent and processing map showed that more than one softening mechanism influenced the deformation of Ti–6Al–1V–3Fe. Additionally, similar mechanisms that are responsible for softening in most titanium alloys are also found in the Ti–6Al–1V–3Fe alloy. Bodunrin et al. [57], Guo et al. [74,75] and Ding et al. [76] showed that typical softening mechanisms are dynamic recovery, dynamic recrystallisation and dynamic transformation especially in the safe working zone. The processing map specifically showed that dynamic recovery and dynamic recrystallisation are the dominant mechanisms in the safe region while cracking and void formation were shown in region of unstable deformation. Cracking and void formation have been established as typical failure mechanisms in titanium alloys with a fully lamellar initial microstructure [32,77]. Dynamic phase transformation has often been reported as one of the mechanisms influencing softening of dual phase titanium alloys. However, this was not given much consideration in this study, since Guo et al. [74,75] explained that dynamic phase transformation of alpha to beta phase is less likely in a fully lamellar initial microstructure than in a fully equiaxed initial microstructure.

Detailed microstructural analysis also showed that dynamic globularisation, otherwise known as geometric dynamic recrystallisation, occurred at low strain rates and high deformation temperatures. This mechanism is well established in commercial Ti–6Al–4V and other titanium alloys with fully lamellar microstructure [32,77]. The classical dynamic globularisation process was explained using two models, the beta penetration model and the lath shear model [53,78,79], with an increasingly wider acceptance of the lath shear model. In this model the occurrence of dynamic globularisation follows four basic steps which include “laths shearing, dislocation generation in the line of shear,

nucleation of dislocation interfaces and migration of interface". These steps are fully described in previous works [79,80].

Some of the observations noted in this study were also reported elsewhere [81] for hot worked Ti-4.5Al–1V–3Fe, another α+β alloy that was investigated by the authors. However, the slight difference in the aluminium content (1.5 wt%) between the two alloys resulted in some variations in the response of the alloys to imposed hot working parameters. One of the notable differences is that Ti–6Al–1V–3Fe showed higher resistance to deformation when compared with Ti-4.5Al–1V–3Fe alloy because the peak flow stress, stress exponent and activation energy were higher under all deformation conditions. The power dissipation efficiency at the optimum working condition was lower in Ti–6Al–1V–3Fe alloy (50%) in comparison with Ti-4.5Al–1V–3Fe alloy (68%). This corroborates higher deformation resistance exhibited by the Ti–6Al–1V–3Fe alloy. Another difference is that the alloys displayed different softening mechanisms at their respective optimum hot working conditions. Dynamic recrystallisation of the prior beta grains was the dominant softening mechanism at ~900°□ and 0.1 s^{-1} in Ti–6Al–1V–3Fe, while dynamic globularisation of the alpha phase was the main softening mechanism at 890 – 905 °□ and 0.003–0.01 s^{-1} in the Ti-4.5Al–1V–3Fe alloy. Although Ti–6Al–1V–3Fe alloy also showed the occurrence of dynamic globularisation of the alpha phase, it only became conspicuous in this alloy at strain rates lower than 0.1 s^{-1}. When the processing maps of both alloys were compared, the unstable deformation region differs for both alloys, 770 – 780 °□ and 1.5 – 10 s^{-1} in this current work, but 875 – 930 °□ and 0.15 – 0.4 s^{-1} in the Ti-4.5Al–1V–3Fe alloy. The marked differences in the behaviour of these similar alloys clearly indicate that even for the same titanium alloy type, hot workability in titanium alloys is sensitive to slight changes in alloy compositions and this has to be put into consideration during large scale manufacturing of titanium-based components.

5. Conclusions

Lower cost titanium alloys for typical land-based applications were designed using the composition of Ti–6Al–4V as the base. Vanadium was partially and fully substituted by iron in Ti–6Al-*x*V-*y*Fe (where $y = 4 - x$, and $x = 0$–4). The effect of this on microstructure and the hot working behaviour of alloys containing partially substituted vanadium was evaluated. The following conclusions were reached.

TiFe and Ti_2Fe intermetallic compounds, which have deleterious effects on the ductility and toughness titanium alloys, were not found in the experimental alloys. The Thermo-Calc predictions were consistent with observations from XRD and microstructural analysis.

The Ti–6Al–1V–3Fe alloy showed similar hot working characteristics to other titanium (α+β) alloys with a fully lamellar structure but had a larger processing window. The most advantageous processing parameters for hot working Ti–6Al–1V–3Fe were ~900 °C and 0.1 s^{-1}. The dominant softening mechanism in this region is dynamic recrystallisation of prior beta grains. Dynamic globularisation of the alpha laths was also seen at temperatures above 850 °C and strain rates below 0.1 s^{-1}. The unsafe region (750 – 780 °C and 1.5 – 10 s^{-1}), where cracking provided the softening mechanism, should be avoided during processing of the alloy. In comparison with Ti-4.5Al–1V–3Fe, a similar low-cost alloy, the Ti–6Al–1V–3Fe had higher deformation resistance due to the slight difference in aluminium content.

Since Ti–6Al–1V–3Fe showed promise in terms of cost reduction via a change in alloy chemistry, and in terms of hot working, future work will consider comparing room temperature mechanical properties with commercial Ti–6Al–4V.

Data availability

The raw/processed data required to reproduce these findings cannot be shared at this time as the data also forms part of an ongoing study.

Declaration of competing interest

The authors declare that they have no known competing financial interests or personal relationships that could have appeared to influence the work reported in this paper.

CRediT authorship contribution statement

Michael O. Bodunrin: Conceptualization, Methodology, Writing - original draft, Writing - review & editing, Funding acquisition. **Lesley H. Chown:** Supervision, Writing - review & editing, Conceptualization, Methodology, Resources, Funding acquisition. **Josias W. van der Merwe:** Supervision, Resources. **Kenneth K. Alaneme:** Supervision.

Acknowledgements

This work was supported through the AESA-RISE Fellowship Programme [ARPDF 18-03], African Materials Science and Engineering Network (A Carnegie-IAS RISE network) and the DST-NRF Centre of Excellence in Strong Materials. AESA-RISE is an independent funding scheme of the African Academy of Sciences (AAS) implemented with the support of Carnegie Corporation of New York. At The AAS, AESA-RISE is implemented through AESA, the Academy's agenda and programmatic platform, created in collaboration with the African Union Development Agency (AUDA-NEPAD). The views expressed in this publication are those of the author(s) and not necessarily those of the AAS, AUDA-NEPAD or Carnegie Corporation.

Appendix A. Supplementary data

Supplementary data to this article can be found online at https://doi.org/10.1016/j.msea.2020.139622.

References

[1] F.H.S. Froes, M.N. Gungor, M.A. Imam, Cost-affordable titanium: the component fabrication perspective, J. Occup. Med. 59 (2007) 28–31, https://doi.org/10.1007/s11837-007-0074-8.
[2] F.H.(Sam) Froes, H. Friedrich, J. Kiese, D. Bergoint, Titanium in the family automobile: the cost challenge, J. Occup. Med. 56 (2004) 40–44.
[3] C. Leyens, M. Peters, Titanium and Titanium Alloys: Fundamentals and Application, WILEY-VCH, Germany, 2003.
[4] M.J. Donachie, Titanium: A Technical Guide, second ed., ASM International, 2000.
[5] B. Dutta, F.H.(Sam, Froes, The Additive Manufacturing (AM) of titanium alloys, Met. Powder Rep. 72 (2017) 96–106, https://doi.org/10.1016/j.mprp.2016.12.062.
[6] K. Faller, F.H. Froes, The use of titanium in family automobiles: current trends, J. Occup. Med. 53 (2001) 27–28.
[7] F.H. Froes, The production of low-cost titanium powders, J. Occup. Med. 50 (1998) 41–43, https://doi.org/10.1007/s11837-998-0413-4.
[8] H. Fujii, K. Takahashi, Development of High Performance Ti-Fe-Al Alloy Series, NIPPON STEEL, 2002. http://www.nssmc.com/en/tech/report/nsc/pdf/8521.pdf. (Accessed 22 November 2016).
[9] D.B. Lee, K.B. Park, H.W. Jeong, S.E. Kim, Mechanical and oxidation properties of Ti–xFe–ySi alloys, Mater. Sci. Eng. 328 (2002) 161–168.
[10] T. Fujita, A. Ogawa, C. Ouchi, H. Tajima, Microstructure and properties of titanium alloy produced in the newly developed blended elemental powder metallurgy process, Mater. Sci. Eng. 213 (1996) 148–153, https://doi.org/10.1016/0921-5093(96)10232-X.
[11] H. Fujii, K. Fujisawa, M. Ishil, Y. Yamashita, Development of Low-Cost High-Strength Ti-Fe-O-N Alloy Series, NIPPON STEEL, 2002. http://www.nssmc.com/en/tech/report/nsc/pdf/8520.pdf. (Accessed 22 November 2016).
[12] L. Bolzoni, E.M. Ruiz-Navas, E. Gordo, Understanding the properties of low-cost iron-containing powder metallurgy titanium alloys, Mater. Des. 110 (2016) 317–323, https://doi.org/10.1016/j.matdes.2016.08.010.
[13] P.G. Esteban, E.M. Ruiz-Navas, L. Bolzoni, E. Gordo, Low-cost titanium alloys? Iron may hold the answers, Met. Powder Rep. 63 (2008) 24–27, https://doi.org/10.1016/S0026-0657(09)70040-2.
[14] N.S. Weston, M. Jackson, FAST-forge – A new cost-effective hybrid processing route for consolidating titanium powder into near net shape forged components, J. Mater. Process. Technol. 243 (2017) 335–346, https://doi.org/10.1016/j.jmatprotec.2016.12.013.
[15] X. Xu, P. Nash, D. Mangabhai, Characterization and sintering of Armstrong process titanium powder, J. Occup. Med. 69 (2017) 770–775, https://doi.org/10.1007/s11837-016-2238-x.

[16] L.L. Benson, I. Mellor, M. Jackson, Direct reduction of synthetic rutile using the FFC process to produce low-cost novel titanium alloys, J. Mater. Sci. 51 (2016) 4250–4261, https://doi.org/10.1007/s10853-015-9718-1.
[17] P.G. Esteban, L. Bolzoni, E.M. Ruiz-Navas, E. Gordo, PM processing and characterisation of Ti–7Fe low cost titanium alloys, Powder Metall. 54 (2011) 242–252, https://doi.org/10.1179/174329009X457063.
[18] L. Bolzoni, E. Herraiz, E.M. Ruiz-Navas, E. Gordo, Study of the properties of low-cost powder metallurgy titanium alloys by 430 stainless steel addition, Mater. Des. 60 (2014) 628–636, https://doi.org/10.1016/j.matdes.2014.04.019.
[19] N.A. Nochovnaya, A.V. Isaichev, V.G. Antashev, Foundations of the development of economically alloyed widely applicable titanium alloys, Mater. Sci. 44 (2008) 396–399, https://doi.org/10.1007/s11003-008-9081-3.
[20] G. Lütjering, J.C. Williams, Engineering Materials: Titanium, Second, Springer, Berlin Heidelberg Newyork, 2007.
[21] M.O. Bodunrin, L.H. Chown, J.W. van der Merwe, K.K. Alaneme, Corrosion behaviour of Ti-Al-xV-yFe experimental alloys in 3.5 wt% NaCl and 3.5 M H2SO4, Mater, Corrosion 69 (2018) 770–780, https://doi.org/10.1002/maco.201709709.
[22] D.J. Prozesky, M.O. Bodunrin, L.H. Chown, Hot-deformation behaviour of α+β Ti-Al-V-Fe experimental alloys, AIP Conf. Proc. 1896 (2017) 160019, https://doi.org/10.1063/1.5008194.
[23] M.O. Bodunrin, Hot Deformation and Corrosion Behaviour of Low-Cost α+β Titanium Alloys with Aluminium, Vanadium and Iron Additions, Thesis, 2018. http://wiredspace.wits.ac.za/handle/10539/26579. (Accessed 26 July 2019).
[24] I. Weiss, S.L. Semiatin, Thermomechanical processing of alpha titanium alloys—an overview, Mater. Sci. Eng. 263 (1999) 243–256, https://doi.org/10.1016/S0921-5093(98)01155-1.
[25] D. Eylon, A. Vassel, Y. Combres, R.R. Boyer, P.J. Bania, R.W. Schutz, Issues in the development of beta titanium alloys, J. Occup. Med. 46 (1994) 14–15, https://doi.org/10.1007/BF03220741.
[26] J.D. Cotton, R.D. Briggs, R.R. Boyer, S. Tamirisakandala, P. Russo, N. Shchetnikov, J.C. Fanning, State of the art in beta titanium alloys for airframe applications, J. Occup. Med. 67 (2015) 1281–1303, https://doi.org/10.1007/s11837-015-1442-4.
[27] B. Roebuck, J.D. Lord, M. Brooks, M.S. Loveday, C.M. Sellars, R.W. Evans, Measurement of flow stress in hot axisymmetric compression tests, Mater. A. T. High. Temp. 23 (2006) 59–83, https://doi.org/10.1179/mht.2006.005.
[28] C. Zener, J.H. Hollomon, Effect of strain rate upon plastic flow of steel, J. Appl. Phys. 15 (1944) 22–32, https://doi.org/10.1063/1.1707363.
[29] H.J. McQueen, N.D. Ryan, Constitutive analysis in hot working, Mater. Sci. Eng. 322 (2002) 43–63, https://doi.org/10.1016/S0921-5093(01)01117-0.
[30] Y.C. Lin, X.-M. Chen, A critical review of experimental results and constitutive descriptions for metals and alloys in hot working, Mater. Des. 32 (2011) 1733–1759, https://doi.org/10.1016/j.matdes.2010.11.048.
[31] Y.V.R.K. Prasad, H.L. Gegel, S.M. Doraivelu, J.C. Malas, J.T. Morgan, K.A. Lark, D. R. Barker, Modeling of dynamic material behavior in hot deformation: forging of Ti-6242, Metall. Trans. A. 15 (1984) 1883–1892, https://doi.org/10.1007/BF02664902.
[32] Y.V.R.K. Prasad, K.P. Rao, S. Sasidhara, Hot Working Guide : a Compendium of Processing Maps, ASM International, 2015.
[33] S.V.S.N. Murty, B.N. Rao, B.P. Kashyap, Development and validation of a processing map for zirconium alloys, Model. Simulat. Mater. Sci. Eng. 10 (2002) 503, https://doi.org/10.1088/0965-0393/10/5/303.
[34] S.V.S. Narayana Murty, B. Nageswara Rao, B.P. Kashyap, Instability criteria for hot deformation of materials, Int. Mater. Rev. 45 (2000) 15–26, https://doi.org/10.1179/095066000771048782.
[35] X. Ma, W. Zeng, B. Xu, Y. Sun, C. Xue, Y. Han, Characterization of the hot deformation behavior of a Ti–22Al–25Nb alloy using processing maps based on the Murty criterion, Intermetallics 20 (2012) 1–7, https://doi.org/10.1016/j.intermet.2011.08.027.
[36] I. Polmear, D. StJohn, J.-F. Nie, M. Qian, 7 - titanium alloys. Light Alloys, fifth ed., Butterworth-Heinemann, Boston, 2017, pp. 369–460, https://doi.org/10.1016/B978-0-08-099431-4.00007-5.
[37] M. Koike, Q. Guo, M. Brezner, H. Fujii, T. Okabe, Mechanical properties of cast Ti-Fe-O-N alloys, J. ASTM Int. (JAI) 2 (2005) 1–10, https://doi.org/10.1520/JAI12781.
[38] A. Safdar, L.-Y. Wei, A. Snis, Z. Lai, Evaluation of microstructural development in electron beam melted Ti-6Al-4V, Mater. Char. 65 (2012) 8–15, https://doi.org/10.1016/j.matchar.2011.12.008.
[39] I. Kopova, J. Stráský, P. Harcuba, M. Landa, M. Janeček, L. Bačákova, Newly developed Ti–Nb–Zr–Ta–Si–Fe biomedical beta titanium alloys with increased strength and enhanced biocompatibility, Mater. Sci. Eng. C 60 (2016) 230–238, https://doi.org/10.1016/j.msec.2015.11.043.
[40] J. Matyka, F. Faudot, J. Bigot, Study of iron solubility in α titanium, Scripta Metall. 13 (1979) 645–648.
[41] F.J. Gil, J.A. Planell, Behaviour of normal grain growth kinetics in single phase titanium and titanium alloys, Mater. Sci. Eng. 283 (2000) 17–24, https://doi.org/10.1016/S0921-5093(00)00731-0.
[42] F.J. Gil, M.P. Ginebra, J.M. Manero, J.A. Planell, Formation of α-Widmanstätten structure: effects of grain size and cooling rate on the Widmanstätten morphologies and on the mechanical properties in Ti6Al4V alloy, J. Alloys Compd. 329 (2001) 142–152, https://doi.org/10.1016/S0925-8388(01)01571-7.
[43] Y.Y. Zong, D.B. Shan, M. Xu, Y. Lv, Flow softening and microstructural evolution of TC11 titanium alloy during hot deformation, J. Mater. Process. Technol. 209 (2009) 1988–1994, https://doi.org/10.1016/j.jmatprotec.2008.04.063.
[44] T.E. Mitchell, J.P. Hirth, A. Misra, Apparent activation energy and stress exponent in materials with a high Peierls stress, Acta Mater. 50 (2002) 1087–1093, https://doi.org/10.1016/S1359-6454(01)00409-8.
[45] H. Chen, C. Cao, Characterization of hot deformation microstructures of alpha-beta titanium alloy with equiaxed structure, Trans. Nonferrous Metals Soc. China 22 (2012) 503–509, https://doi.org/10.1016/S1003-6326(11)61205-3.
[46] V.V. Balasubrahmanyam, Y.V.R.K. Prasad, Deformation behaviour of beta titanium alloy Ti–10V–4.5Fe–1.5Al in hot upset forging, Mater. Sci. Eng. 336 (2002) 150–158, https://doi.org/10.1016/S0921-5093(01)01982-7.
[47] Y. Zhang, L. Huang, B. Liu, L. Geng, Hot deformation behavior of in-situ TiBw/Ti6Al4V composite with novel network reinforcement distribution, Trans. Nonferrous Metals Soc. China 22 (2012) s465–s471, https://doi.org/10.1016/S1003-6326(12)61747-6.
[48] Q. Guo-Zheng, W. Yang, L. Ying-Ying, Z. Jie, Effect of temperatures and strain rates on the average size of grains refined by dynamic recrystallization for as-extruded 42CrMo steel, Mater. Res. 16 (2013) 1092–1105, https://doi.org/10.1590/S1516-14392013005000091.
[49] I. Philippart, H.J. Rack, High temperature dynamic yielding in metastable Ti–6.8 Mo–4.5 F–1.5 Al, Mater. Sci. Eng. 243 (1998) 196–200.
[50] I. Weiss, S.L. Semiatin, Thermomechanical processing of beta titanium alloys—an overview, Mater. Sci. Eng. 243 (1998) 46–65, https://doi.org/10.1016/S0921-5093(97)00783-1.
[51] W. Peng, W. Zeng, Q. Wang, H. Yu, Characterization of high-temperature deformation behavior of as-cast Ti60 titanium alloy using processing map, Mater. Sci. Eng. 571 (2013) 116–122, https://doi.org/10.1016/j.msea.2013.01.008.
[52] W. Peng, W. Zeng, Q. Wang, H. Yu, Comparative study on constitutive relationship of as-cast Ti60 titanium alloy during hot deformation based on Arrhenius-type and artificial neural network models, Mater. Des. 51 (2013) 95–104, https://doi.org/10.1016/j.matdes.2013.04.009.
[53] C. Wu, H. Yang, X. Fan, Z. Sun, Dynamic globularisation kinetics during hot working of TA15 titanium alloy with colony microstructure, Trans. Nonferrous Metals Soc. China 21 (2011), https://doi.org/10.1016/S1003-6326(11)60957-6, 1963–1969.
[54] H. Song, S. Zhang, M. Cheng, Dynamic globularisation prediction during cogging process of large size TC11 titanium alloy billet with lamellar structure, Def. Technol. 10 (2014) 40–46, https://doi.org/10.1016/j.dt.2014.01.003.
[55] X.F. Bai, Y.Q. Zhao, W.D. Zeng, Z.Q. Jia, Y.S. Zhang, Characterization of hot deformation behavior of a biomedical titanium alloy TLM, Mater. Sci. Eng. 598 (2014) 236–243, https://doi.org/10.1016/j.msea.2014.01.005.
[56] R.L. Goetz, S.L. Semiatin, The adiabatic correction factor for deformation heating during the uniaxial compression test, J. Mater. Eng. Perform. 10 (2001) 710–717, https://doi.org/10.1361/105994901770344593.
[57] M.O. Bodunrin, L.H. Chown, J.W. van der Merwe, K.K. Alaneme, Hot working of Ti-6Al-4V with a complex initial microstructure, Int. J. Material Form. (2018), https://doi.org/10.1007/s12289-018-1457-9.
[58] P.M. Souza, H. Beladi, R. Singh, B. Rolfe, P.D. Hodgson, Constitutive analysis of hot deformation behavior of a Ti6Al4V alloy using physical based model, Mater. Sci. Eng. 648 (2015) 265–273, https://doi.org/10.1016/j.msea.2015.09.055.
[59] P.M. Souza, H. Beladi, B. Rolfe, R. Singh, P.D. Hodgson, Softening behavior of Ti6Al4V alloy during hot deformation, in: Mater. Sci. Forum, Materials Science Forum, Port Elizabeth, South Africa, 2015, pp. 407–412. https://doi.org/10.4028/www.scientific.net/MSF.828-829.407.
[60] S.L. Semiatin, V. Seetharaman, I. Weiss, Flow behavior and globularisation kinetics during hot working of Ti–6Al–4V with a colony alpha microstructure, Mater. Sci. Eng. 263 (1999) 257–271, https://doi.org/10.1016/S0921-5093(98)01156-3.
[61] L. Briottet, J.J. Jonas, F. Montheillet, A mechanical interpretation of the activation energy of high temperature deformation in two phase materials, Acta Mater. 44 (1996) 1665–1672, https://doi.org/10.1016/1359-6454(95)00257-X.
[62] H. Mirzadeh, Simple physically-based constitutive equations for hot deformation of 2024 and 7075 aluminum alloys, Trans. Nonferrous Metals Soc. China 25 (2015) 1614–1618, https://doi.org/10.1016/S1003-6326(15)63765-7.
[63] H. Mirzadeh, Constitutive modeling and prediction of hot deformation flow stress under dynamic recrystallization conditions, Mech. Mater. 85 (2015) 66–79, https://doi.org/10.1016/j.mechmat.2015.02.014.
[64] T. Seshacharyulu, S.C. Medeiros, W.G. Frazier, Y.V.R.K. Prasad, Microstructural mechanisms during hot working of commercial grade Ti–6Al–4V with lamellar starting structure, Mater. Sci. Eng. 325 (2002) 112–125, https://doi.org/10.1016/S0921-5093(01)01448-4.
[65] J.K. Fan, H.C. Kou, M.J. Lai, B. Tang, H. Chang, J.S. Li, Hot deformation mechanism and microstructure evolution of a new near β titanium alloy, Mater. Sci. Eng. 584 (2013) 121–132, https://doi.org/10.1016/j.msea.2013.07.019.
[66] Y.V.R.K. Prasad, T. Seshacharyulu, Modelling of hot deformation for microstructural control, Int. Mater. Rev. 43 (1998) 243–258, https://doi.org/10.1179/imr.1998.43.6.243.
[67] C. Poletti, L. Germain, F. Warchomicka, M. Dikovits, S. Mitsche, Unified description of the softening behavior of beta-metastable and alpha+beta titanium alloys during hot deformation, Mater. Sci. Eng. 651 (2016) 280–290, https://doi.org/10.1016/j.msea.2015.10.109.
[68] I. Balasundar, K.R. Ravi, T. Raghu, On the high temperature deformation behaviour of titanium alloy BT3-1, Mater. Sci. Eng. 684 (2017) 135–145, https://doi.org/10.1016/j.msea.2016.12.043.
[69] Y.C. Zhu, W.D. Zeng, J.L. Liu, Y.Q. Zhao, Y.G. Zhou, H.Q. Yu, Effect of processing parameters on the hot deformation behavior of as-cast TC21 titanium alloy, Mater. Des. 33 (2012) 264–272, https://doi.org/10.1016/j.matdes.2011.07.018.
[70] D. He, J.C. Zhu, Z.H. Lai, Y. Liu, X.W. Yang, An experimental study of deformation mechanism and microstructure evolution during hot deformation of

Ti–6Al–2Zr–1Mo–1V alloy, Mater. Des. 46 (2013) 38–48, https://doi.org/10.1016/j.matdes.2012.09.045.
[71] B. Perumal, M.A. Rist, S. Gungor, J.W. Brooks, M.E. Fitzpatrick, The effect of hot deformation parameters on microstructure evolution of the α-phase in Ti-6Al-4V, Metall. Mater. Trans. 47 (2016) 4128–4136, https://doi.org/10.1007/s11661-016-3552-1.
[72] J.-M. Oh, B.-G. Lee, S.-W. Cho, S.-W. Lee, G.-S. Choi, J.-W. Lim, Oxygen effects on the mechanical properties and lattice strain of Ti and Ti-6Al-4V, Met. Mater. Int. 17 (2011) 733–736, https://doi.org/10.1007/s12540-011-1006-2.
[73] C.J. Bettles, D. Tomus, M.A. Gibson, The role of microstructure in the mechanical behaviour of Ti–1.6 wt.%Fe alloys containing O and N, Mater. Sci. Eng. 528 (2011) 4899–4909, https://doi.org/10.1016/j.msea.2011.03.030.
[74] B. Guo, S.L. Semiatin, J.J. Jonas, Dynamic transformation during the high temperature deformation of two-phase titanium alloys, Mater. Sci. Eng. 761 (2019) 138047, https://doi.org/10.1016/j.msea.2019.138047.
[75] B. Guo, S.L. Semiatin, J.J. Jonas, S. Yue, Dynamic transformation of Ti–6Al–4V during torsion in the two-phase region, J. Mater. Sci. (2018) 1–11, https://doi.org/10.1007/s10853-018-2237-0.
[76] R. Ding, Z.X. Guo, A. Wilson, Microstructural evolution of a Ti–6Al–4V alloy during thermomechanical processing, Mater. Sci. Eng. 327 (2002) 233–245.
[77] T. Seshacharyulu, S.C. Medeiros, W.G. Frazier, Y.V.R.K. Prasad, Microstructural mechanisms during hot working of commercial grade Ti–6Al–4V with lamellar starting structure, Mater. Sci. Eng. 325 (2002) 112–125, https://doi.org/10.1016/S0921-5093(01)01448-4.
[78] J.K. Fan, H.C. Kou, M.J. Lai, B. Tang, H. Chang, J.S. Li, Hot deformation mechanism and microstructure evolution of a new near β titanium alloy, Mater. Sci. Eng. 584 (2013) 121–132, https://doi.org/10.1016/j.msea.2013.07.019.
[79] J.K. Fan, H.C. Kou, M.J. Lai, B. Tang, H. Chang, J.S. Li, Characterization of hot deformation behavior of a new near beta titanium alloy: Ti-7333, Mater. Des. 49 (2013) 945–952, https://doi.org/10.1016/j.matdes.2013.02.044.
[80] X.G. Fan, Y. Zhang, P.F. Gao, Z.N. Lei, M. Zhan, Deformation behavior and microstructure evolution during hot working of a coarse-grained Ti-5Al-5Mo-5V-3Cr-1Zr titanium alloy in beta phase field, Mater. Sci. Eng. 694 (2017) 24–32, https://doi.org/10.1016/j.msea.2017.03.095.
[81] M.O. Bodunrin, L.H. Chown, J.W. van der Merwe, K.K. Alaneme, Hot working behaviour of experimental Ti-4.5Al-1V-3Fe alloy with initial lamellar microstructure, Int. J. Adv. Manuf. Technol. 106 (2020) 1901–1916, https://doi.org/10.1007/s00170-019-04718-7.